Earth and Planetary Science Letters 409 (2015) 265–277

Contents lists available at ScienceDirect

Earth and Planetary Science Letters

www.elsevier.com/locate/epsl

Density-depth model of the continental wedge at the maximum slip segment of the Maule Mw8.8 megathrust earthquake

Andrei Maksymowicz [a,b,*], Anne M. Tréhu [c], Eduardo Contreras-Reyes [a], Sergio Ruiz [a]

[a] Departamento de Geofísica, Facultad de Ciencias Físicas y Matemáticas, Universidad de Chile, Santiago, Chile
[b] Departamento de Geología, Facultad de Ciencias Físicas y Matemáticas, Universidad de Chile, Santiago, Chile
[c] College of Earth, Ocean and Atmospheric Sciences, Oregon State University, Corvallis, OR, USA

ARTICLE INFO

Article history:
Received 30 April 2014
Received in revised form 15 September 2014
Accepted 4 November 2014
Available online 25 November 2014
Editor: P. Shearer

Keywords:
marine gravity
density modeling
megathrust earthquake
continental wedge
subducted seamount

ABSTRACT

Complexities in the rupture process during a megathrust earthquake can be attributed to the combined effect of inhomogeneous distribution of stress accumulated during the interseismic period and inhomogeneous rheology of the seismogenic contact. We modeled the free-air gravity field of the southern Central Chile convergent margin along five 2-D profiles that cross the patch of highest slip during the Chilean 2010 megathrust earthquake in order to analyze variability in the density and shape of the continental wedge and its relationship with seismotectonics. We also analyzed the bathymetry to derive the long-term interplate friction coefficient. The results show that the high slip patch during the Maule earthquake corresponds to a segment of the margin characterized by (1) low densities in the continental wedge, (2) low vertical loading over the inter-plate contact, (3) a well-developed shelf basin and, (4) low taper angles consistent with a low effective basal friction coefficient. We interpret the correlation between these parameters in terms of the total potential energy change during the earthquake and conclude that if the normal stress or frictional coefficient are low, then a large slip does not necessarily imply a large amount of coseismic work. Heterogeneities in density of the continental basement can therefore be related to complexities in the pattern of coseismic slip and in the aftershock distribution. Locally, a subducted seamount or seaward spur of high-density continental crust may be present near the high slip patch.

1. Introduction

Numerous authors have identified a close relationship between the inhomogeneous slip distribution during megathrust earthquakes and the rheology of the continental wedge and subducted slab. Byrne et al. (1988) noted a correlation between the up-dip limit of seismogenic slip at accretionary margins and the backstop, defined here as the contact between the accretionary prism and the older, stiffer forearc basement rock. This observation has led to the suggestion that low friction beneath the accretionary prism can act as a barrier during coseismic slip propagation (Pacheco et al., 1993; Nakanishi et al., 2002; Contreras-Reyes et al., 2010). It has also been suggested that dewatering, lithification and metamorphism of marine sediments may allow for seismogenic rupture propagation into the accretionary complex (e.g. Hyndman et al., 1997; Gutscher and Peacock, 2003; Gulick et al., 2011).

Heterogeneity in slip along strike has also been observed landward of the backstop. Wells et al. (2003) and Song and Simon (2003) noted a correlation between the location of the maximum slip distribution during megathrust earthquakes and slope basins defined by gravity lows at a number of Circum-Pacific subduction zones and suggested that the development of these basins is related to basal erosion resulting from high shear stresses, which result in subsidence over asperities in the seismogenic contact. In addition, along-strike inhomogeneities in slip distribution during earthquakes have been associated in many places with the presence of subducted oceanic features (seamounts, ridges, fracture zones and the crustal faulting of the slab), which may act as barriers and/or asperities on the seismogenic contact (e.g. Aki, 1979; Cloos, 1992; Das and Watts, 2009; Sparkes et al., 2010; Contreras-Reyes and Carrizo, 2011; Muller and Landgrebe, 2012; Álvarez et al., 2014).

According to critical Coulomb wedge theory (Davis et al., 1983; Dahlen et al., 1984; Dahlen, 1984), the basal friction at the base of the continental wedge is a key parameter controlling the long-term deformation style at the convergent margins. This theory predicts that low seafloor slope angles should be associated with

* Corresponding author at: Departamento de Geofísica, Facultad de Ciencias Físicas y Matemáticas, Universidad de Chile, Blanco Encalada 2002, Santiago, Chile.
E-mail address: andrei@dgf.uchile.cl (A. Maksymowicz).

http://dx.doi.org/10.1016/j.epsl.2014.11.005
0012-821X/

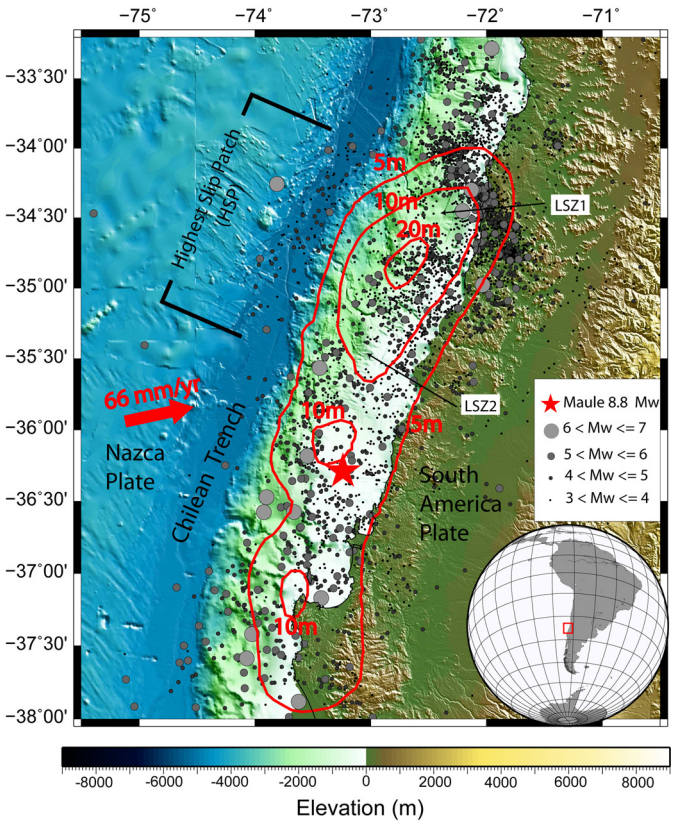

Fig. 1. Rupture area of the Maule Mw8.8 earthquake, and the regional bathymetry/topography. The red star shows to the epicenter of the Maule earthquake determined by the Centro Sismológico Nacional, University of Chile (CSN). The gray circles show aftershock seismicity for one year after the main event (also located by CSN). The red curves correspond to iso-contours of slip during the Maule earthquake according to Moreno et al. (2012). Black arrows show two zones characterized by low rate of aftershock seismicity (LSZ1 and LSZ2). (For interpretation of the references to color in this figure legend, the reader is referred to the web version of this article.)

low basal friction. Hence, along-strike changes in the slope angle could be indicative of the spatial variability in the long-term basal friction. Moreover, along-strike changes in the density of the continental wedge due to geological structure could modify the normal stress on the interplate contact (Scholz and Campos, 1995; Tassara, 2010).

To obtain insights into factors influencing coseismic rupture, we modeled gravity anomalies in the region of maximum slip during the 2010 Maule earthquake on the South-Central Chilean margin (Lay et al., 2010; Lorito et al., 2011; Luttrell et al., 2011; Moreno et al., 2012) to determine whether the weight of the overlying plate was correlated with the maximum magnitude of slip distribution. We also examined seafloor morphology in the context of critical wedge theory to determine whether morphology and density were correlated.

2. Seismotectonic setting

Our study area is the Nazca–South America convergent margin between ∼33.5°S and ∼36°S (Fig. 1). This segment of the margin corresponds to the northern portion of the rupture area associated to the Chilean 2010 megathrust earthquake (Maule Mw8.8 earthquake). The rupture area (from ∼34°S to ∼38°S) covered a seismic gap that had not experienced a large earthquake since 1835 and 1928 (Lomnitz, 1971; Ruegg et al., 2009) and extended from the northern limit of the Valdivia 1960 Mw9.5 earthquake (e.g., Barrientos and Ward, 1990) to the southern limit of the 1985 Mw7.8 earthquake (Comte et al., 1986).

Most of the coseismic slip models indicate that our study area includes the highest slip patch (HSP) for the Maule Mw8.8 earthquake (e.g. Lay et al., 2010; Lorito et al., 2011; Luttrell et al., 2011; Moreno et al., 2012, among others). The main-shock initiated south of this HSP (red star in Fig. 1), and rupture propagated north and south from this hypocenter (Ruiz et al., 2012). Due to differences in the seismological and geodetic databases and in the inversion algorithms used by different authors, details of the slip models for Maule earthquake differ from each other, but their main features are similar. In particular, we observe that the geographic position of the HSP varies by about 50 km, with the model of Luttrell et al. (2011) as the northernmost solution. We use the coseismic slip model of Moreno et al. (2012), which combines GPS and InSAR observations and includes a realistic slab geometry, as a reference for the figures and discussion.

The aftershocks of the Maule earthquake also exhibit a change at the HSP segment. Fig. 1 shows the seismicity located by the National Seismological Center (CSN) of the University of Chile using the land network during the year after the Maule earthquake. Similar features can be observed in the aftershocks located by Hayes et al. (2013), Lange et al. (2012) and Rietbrock et al. (2012). Immediately to the north and south of the HSP, hypocenters are distributed across almost the entire continental wedge, with a westernmost limit near the deformation front and there is little seismicity seaward of the deformation front (Moscoso et al., 2011; Lange et al., 2012; Rietbrock et al., 2012). Within the HSP region, the oceanic plate seaward of the trench has a high level of seismicity, and there is a notable seismic gap beneath the accretionary wedge. Regions of relatively low seismicity (LSZ1 and LSZ2 in Fig. 1) seem to limit the HSP as indicated by the 20 m slip contour.

South of 33°S, the Nazca–South America margin is characterized by tectonic accretion (Díaz-Naveas, 1999; Contreras-Reyes et al., 2010). The trench is sediment filled due to the high terrigenous sediment flux delivered by rivers, submarine landslides, pelagic sediment influx, and the northward redistribution of sediments via the axial channel. At 33°S, the trench is dammed by the Juan Fernandez ridge cutting off much of the northward sediment flux (e.g., Thornburg and Kulm, 1987). Between ∼34°S and ∼35.5°S the morphology of the continental wedge is distinctive: the deformation front swings seaward and the width of the wedge increases, generating a local decrease of the slope angle (Contreras-Reyes et al., 2013).

The cross-sectional area of the accretionary prism in the study region was determined by Moscoso et al. (2011) based on 2D tomography of a wide-angle seismic-refraction profile located at ∼34.5°S. On this profile, the boundary between accreted sediments and framework rock occurs ∼20 km landward from the deformation front. South of ∼34°S, the continental basement observed onshore corresponds to the outcrops of a paired metamorphic belt (Western and Eastern series) that has been interpreted as a late-Paleozoic accretionary prism (Hervé, 1988; Willner et al., 2005). Basement rocks beneath the continental margin probably represent, at least partially, this metamorphic complex.

Reflection seismic profiles in this region (Díaz-Naveas, 1999; Contardo et al., 2008; Contreras-Reyes et al., 2010, 2013) show asymmetric half-graben basins beneath the continental slope and well-developed shelf basins. The geometry of the slope basins is controlled by the displacements on the bordering faults that accommodate differential tectonic subsidence and/or uplift in the continental wedge. The progradational or aggradational sequences that fill the shelf basins are interpreted as the result of the dominant horizontal or vertical growth of the continental wedge (Contardo et al., 2008).

3. Gravity and magnetic anomalies at the Maule Earthquake rupture zone

3.1. Data bases

We analyze free-air gravity and magnetic anomaly grids generated by merging data from the 2012 ChilePEPPER (Project Evaluating Prism Post-Earthquake Response) expedition on the R/V Melville with regional databases. To generate the gravity grid, data acquired during ChilePEPPER were merged with the global gravity model of Sandwell and Smith (2009). The ChilePEPPER data were corrected using the standard process of reduction and leveling, and a constant gravity value was added to the local data to match the median of the ChilePEPPER data with the median of the data of Sandwell and Smith (see Supplementary material for details). After correction of the ChilePEPPER data, the amplitude difference between the two data bases is everywhere less than 10 mGal, which validates the procedure of embedding the high-resolution ship-board data within the global model.

The marine magnetic anomaly map (Fig. 2d) was generated using the magnetic data acquired during ChilePEPPER and additional marine magnetic lines obtained from the GEODAS database (NOAA). In order to correct for temporal variation of the geomagnetic field during ChilePEPPER, we used the time series at the Cerrillos Station (33.50°S, 70.72°W) of the SAMBA project (Cordaro et al., 2012), located ∼250 km northwest of the study area. The final magnetic grid is the result of applying a micro-leveling process to the ChilePEPPER and GEODAS lines (see Supplementary material for details).

For bathymetry/topography, we used an elevation model corresponding to a grid of high-resolution bathymetry data of the studied zone (Flueh and Bialas, 2008). Onshore, we used SRTM topography (90 m resolution, Jarvis et al., 2008).

3.2. Preliminary interpretation

As is expected at subduction margins, the main long wavelength feature of the marine free-air gravity is a trench-parallel negative anomaly associated with the bending of the slab at the outer-rise, the trench basin and the continental slope. This feature presents important latitudinal changes at the studied zone (Fig. 2a). South of ∼35.5°S and north of 34°S, the negative anomaly is approximately symmetrical around the deformation front. Between ∼35.5°S and ∼34°S, and coinciding with the HSP segment, the continental slope landward of the deformation front shows a relative low gravity anomaly, which is correlated with the bathymetry. This correlation between a negative gravity anomaly and the HSP of the Maule earthquake has also been observed by Álvarez et al. (2014) who analyze the long wavelength signal of the vertical gravity gradient derived from the satellite GOCE data.

In order to highlight the short wavelength anomalies of the gravity signal, we apply a vertical gradient filter (Fig. 2b). In the filtered signal, a circular shaped anomaly (R1) becomes evident in the central portion of the HSP. This local feature is observed in a zone of high aftershock seismicity, around the central portion of the HSP area (Fig. 1). The shape and the amplitude of this gravity anomaly are similar to a gravity anomaly near 34.5°S, 73.9°W that corresponds to a seamount on the Nazca plate with a diameter of ∼18 km and height of ∼2 km. We speculate that this anomaly indicates a buried seamount of similar size and will test this hypothesis in the next section. Although lower amplitude circular anomalies are pervasive in the global data set and are likely artifacts, these artifacts are not present in the ChilePEPPER data (Fig. S2) where the R1 anomaly is clearly observable.

The high gravity anomaly observed at the coast near the epicenter (H1) has been correlated with high seismic velocities and was interpreted by Hicks et al. (2012) to be a subducted seamount. We note that the epicenter is also well correlated with a gravity high (anomaly H2) located ∼60 km seaward from the anomaly interpreted by those authors. Although features observed in the gravity signal can be indicative of lateral variations in the subsurface, some features are clearly correlated with bathymetry. To highlight internal density anomalies within the continental wedge, we replaced the ocean by a 3-D body of density 2670 kg/m^3. The result of this water correction process is shown in Fig. 2c. After the water correction, an elongated low gravity anomaly is observed along the axis of the HSP. This gravity low can be interpreted as an evidence of a more developed shelf basin overlying the HSP. This is consistent with a similar correlation observed by Wells et al. (2003) for a number of circum-Pacific earthquakes.

The magnetic grid of the study area (Fig. 2d) shows two distinct domains. Over the oceanic Nazca plate, the anomalies are dominated by the pattern of geomagnetic field inversions, which was generated at the oceanic spreading center. This pattern of linear anomalies, elongated in the northwest direction, extends up to 40 km landward of the deformation front, consistent with the presence of non-magnetic sedimentary material overlying the slab in this region.

Between the landward limit of the accretionary prism and the coast, a second domain of magnetic anomalies is observed. This zone is characterized by a complex distribution of anomalies with lower intensity compared to the Nazca plate domain, which can be interpreted as a response to the variable magnetization of the continental basement combined with increasing depth and temperature of the oceanic plate (Fleming and Tréhu, 1999). A high-amplitude magnetic anomaly (M1) is observed in the northern portion of the HSP zone (blue contour in Fig. 2d). This anomaly is roughly coincident with a zone of low aftershocks seismicity (LSZ1 in Fig. 1) and immediately landward of the gravity anomaly interpreted as a subducted seamount, but without a-priori knowledge of the direction and magnitude of the magnetization, the relation between magnetic and gravity anomalies remains undetermined. None-the-less, this anomaly suggests that there is significant heterogeneity in the paleo-accretionary complex that forms continental basement of the margin in this region.

4. 2-D forward model of gravity

4.1. Algorithm

The 2D and 3D forward modeling algorithms that are often used to model gravity anomalies only allow models constructed from constant-density polygonal blocks. With this formulation, generation of models that include density gradients is difficult. However, independent information (seismic velocity models or densities observed in wells) often suggests the presence of strong density gradients resulting from compaction, changes in lithology and/or thermal variation in the lithosphere. In order to model density gradients within the continental wedge, we developed a 2D forward modeling algorithm (named GravGrad), that allows for rapid modification of the margin geometry and the presence of density discontinuities and gradients in an inhomogeneous layered space.

GravGrad uses the analytical response of a tabular prism with a vertical density gradient that extends to infinity in the direction perpendicular to the profile (see the complete derivation in the Supplementary material). The density within the prism is:

$$\rho(z) = \rho_0 + R(z - z_1) \tag{1}$$

where R is the vertical gradient, z_1 is the depth at the top of the prism, ρ_0 is the density at z_1. This prism extends horizontally from

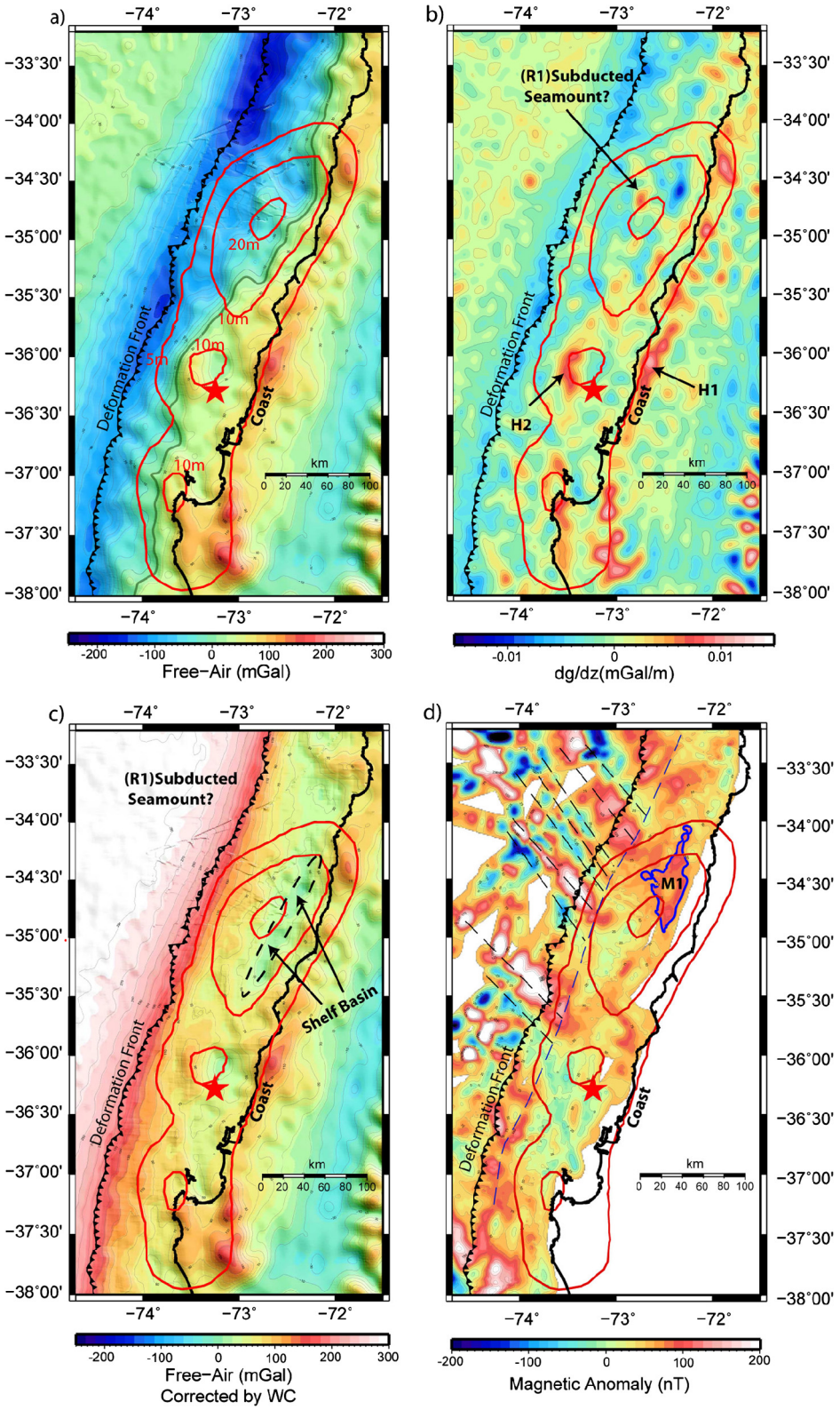

Fig. 2. Gravity and magnetic fields of the Maule earthquake region. In all panels, the iso-slip contours of the Maule earthquake (Moreno et al., 2012) are shown, and the red star indicates the epicenter of the Maule earthquake (located by CSN). **(a)** Free-air gravity field. The grid results from merging the Sandwell and Smith (2009) global grid with the new, high-ChilePEPPER data as described in the supplement. The green line between the deformation front and coast is the iso-contour of 10 mGal. **(b)** First vertical derivative filter applied to the free-air anomaly shown in (a). R1 corresponds to a local high gravity anomaly interpreted as a possible subducted seamount. H1 and H2 are local high gravity anomalies that are spatially correlated with the epicenter of the Maule earthquake (see main text for details). **(c)** Free air anomaly corrected for the effect of the water column (see main text for details). The black dashed line highlights the elongated gravity minimum interpreted as a well-developed shelf basin. **(d)** Magnetic anomaly map of resulting from merging and gridding GEODAS and new ChilePEPPER data. The thin black dashed lines show the orientation of seafloor spreading anomalies on Nazca oceanic plate. The blue dashed line indicates the approximate landward limit of the oceanic magnetic pattern. Magnetic anomaly M1, highlighted by a blue line, corresponds to the highest amplitude magnetic anomaly observed from the marine continental basement in the rupture area. (For interpretation of the references to color in this figure legend, the reader is referred to the web version of this article.)

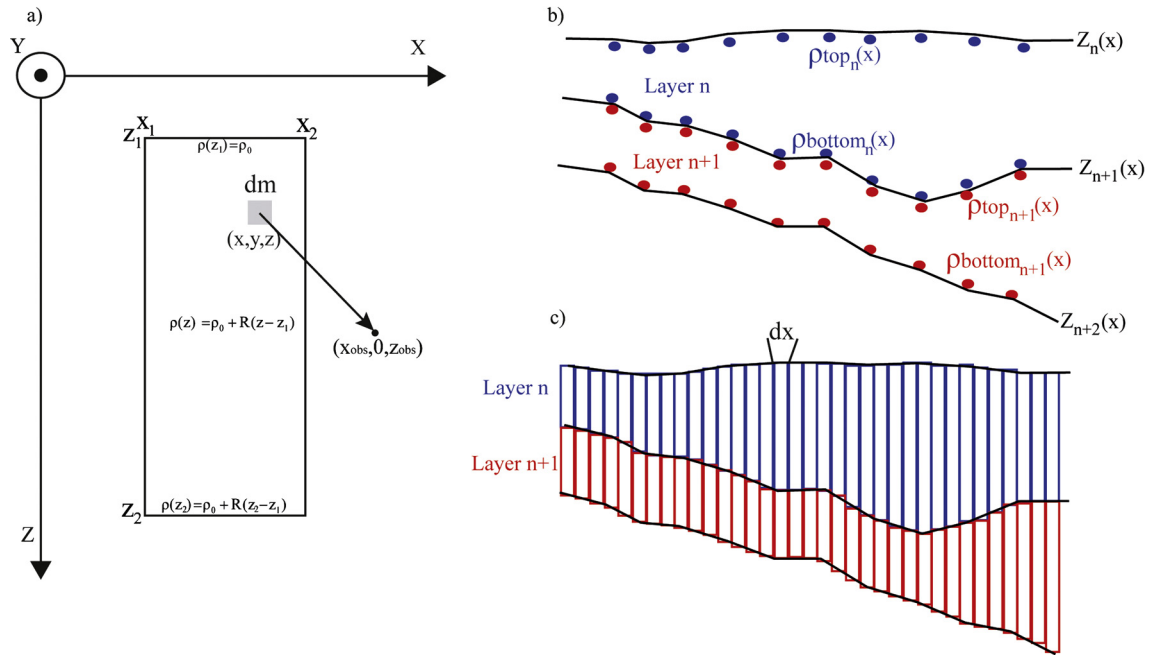

Fig. 3. Graphic schema of the algorithm for the 2-D gravity modeling (GravGrad). **(a)** The 2-D layered medium is discretized using rectangular prisms. Each prism shows a linear gradient in density between the top and the bottom. **(b)** The number and positions of the points that define the interfaces between two layers can be interactively modified. The densities immediately above and immediately below each point of the interfaces can also be interactively modified. **(c)** To calculate the gravity response, the layers and their associated densities are resampled by linear interpolation in order to generate a set of narrow prisms that cover the entire model.

x_1 to x_2 and vertically to z_2. The analytical response of the prism at observing point (x_{obs}, z_{obs}) is:

$$g(x_{obs}, z_{obs}) = G \cdot \rho_0 \cdot A - G \cdot R \cdot z_1 \cdot A - G \cdot R \cdot B \tag{2a}$$

where G is the gravitational constant. A and B are geometrical terms given by:

$$\begin{aligned}
A &= a\left(\ln\left(u_2^2 + a^2\right) - \ln\left(u_1^2 + a^2\right)\right) \\
&\quad + b\left(\ln\left(u_1^2 + b^2\right) - \ln\left(u_2^2 + b^2\right)\right) \\
&\quad + 2u_2\left(\arctan(a/u_2) - \arctan(b/u_2)\right) \\
&\quad + 2u_1\left(\arctan(b/u_1) - \arctan(a/u_1)\right) \\
B &= -az_{obs}\ln\left(u_2^2 + a^2\right) - a^2\arctan(u_2/a) \\
&\quad + \left(u_2^2 - 2u_2z_{obs}\right)\arctan(a/u_2) + au_2 \\
&\quad + az_{obs}\ln\left(u_1^2 + a^2\right) + a^2\arctan(u_1/a) \\
&\quad - \left(u_1^2 - 2u_1z_{obs}\right)\arctan(a/u_1) - au_1 \\
&\quad + bz_{obs}\ln\left(u_2^2 + b^2\right) + b^2\arctan(u_2/b) \\
&\quad - \left(u_2^2 - 2u_2z_{obs}\right)\arctan(b/u_2) - bu_2 \\
&\quad - bz_{obs}\ln\left(u_1^2 + b^2\right) - b^2\arctan(u_1/b) \\
&\quad + \left(u_1^2 - 2u_1z_{obs}\right)\arctan(b/u_2) + bu_1 \\
a &= (x_2 - x_{obs}), \qquad b = (x_1 - x_{obs}), \\
u_1 &= (z_{obs} - z_1), \qquad u_2 = (z_{obs} - z_2)
\end{aligned} \tag{2b}$$

Each layer of the model is defined by discrete functions for the depth of the top, the depth of the bottom, the density at the top, and the density at the bottom of the layer ($z_n(x)$, $z_{n+1}(x)$, $\rho\text{top}_n(x)$, $\rho\text{bottom}_n(x)$, see Fig. 3b). These discrete functions are modified interactively at each step of the forward modeling. To calculate the gravity response, GravGrad resamples those functions in the x direction by linear interpolation using a regular sampling interval (dx) in order to cover the entire space with rectangular prisms of width dx (Fig. 3c). The gravity response of each prism is calculated for the observation point using (2) and the responses are summed. GravGrad has been implemented in FORTRAN90, with auxiliary MATLAB scripts for graphical presentation of model interfaces and predicted gravity anomalies.

4.2. 2-D density models at the studied zone

In order to perform a quantitative analysis of gravity anomalies observed in the HSP area, we selected five profiles perpendicular to the trench and modeled the free-air gravity signal as a function of the density structure (PG1–PG5 in Fig. 4). PG1 and PG5 profiles were selected to be north and south of the HSP, while PG2, PG3 and PG4 cross the HSP. PG3 is coincident with the wide angle seismic profile presented by Moscoso et al. (2011).

The independent geophysical information used to constrain the geometry of the density models is:

(a) The SLAB1 model for the slab shape at the deepest part of the seismogenic contact (Hayes et al., 2012).
(b) Seismic reflection profiles acquired during the ChilePEPPER (Tréhu et al., 2012) and the FONDEF Project DOOI104 (Contardo et al., 2008) for the geometry of the continental wedge near the trench (see navigation in Fig. 4a). Observed two-way travel-times were converted to depth using the velocity model of Moscoso et al. (2011).
(c) The velocity-depth model of Moscoso et al. (2011) for the oceanic crustal thickness, and crust and mantle P-wave velocities. Densities of the oceanic crust, upper mantle and continental wedge were estimated using empirical conversion laws to convert velocity to density (Birch, 1961a, 1961b; Hamilton, 1978).
(d) The depth of the continental Moho (30–35 km) as indicated by the receiver function analysis of Dannowski et al. (2013) near profile PG4 and by the receiver function analysis of Maksymowicz (2007).

As the gravity anomaly at a point is affected by the 3D bathymetry around the point, we generated a representative bathymetry

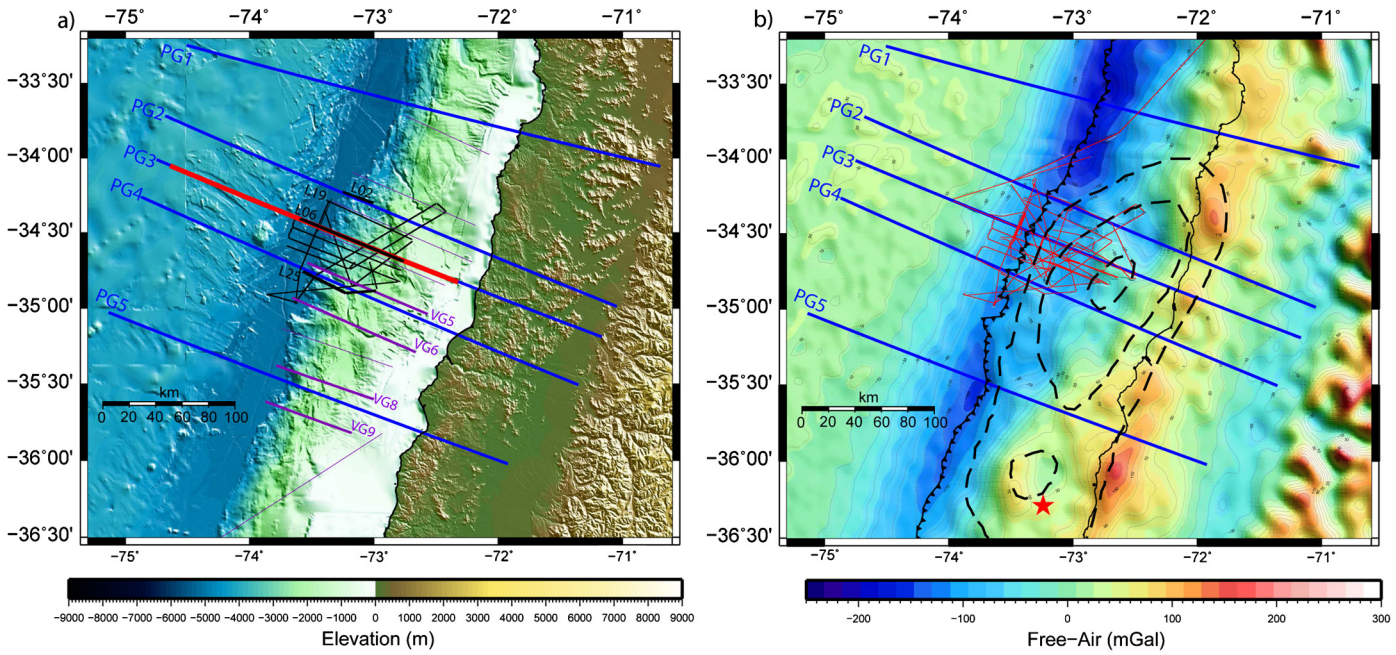

Fig. 4. Location of the five modeled gravity lines. **(a)** Selected gravity lines (PG1 to PG5) and bathymetry/topography of the studied area. The black lines correspond to the reflection seismic lines acquired during ChilePEPPER. The magenta lines are reflection seismic profiles of the FONDEF Project. The red line corresponds to the wide angle refraction profile presented by Moscoso et al. (2011). The highlighted seismic lines (thick lines) were used to constrain the gravity models. **(b)** Selected gravity lines (PG1 to PG5) overlain on the free-air gravity anomaly. Dashed black lines correspond to the iso-slip contours of the Maule earthquake according to Moreno et al. (2012). Red star indicates the epicenter of the Maule earthquake, and thin red lines show the trackline along witch gravity data were acquired during ChilePEPPER. (For interpretation of the references to color in this figure legend, the reader is referred to the web version of this article.)

for each profile by averaging the depth perpendicular to the profile for a distance of 8 km on each side of the profile.

Fig. 5 shows the results of the 2-D forward modeling of the five selected profiles. The RMS obtained in all models is lower than 2.3 mGal, corresponding to ∼1% of the amplitude of the free-air gravity anomaly. To avoid edge effects, the models were extended 10,000 km east and west of the sections shown in Fig. 5 and to a depth of 100 km. The models include 7 layers: (1) the water layer with homogeneous density, (2) the shallow sedimentary unit (pelagic sediments, trench fill, slope basins and shelf basins), (3) the continental wedge unit, (4) the mantle wedge unit (underneath the continental Moho), (5) the upper oceanic crust unit, (6) the lower oceanic crust, and (7) the mantle (from the oceanic Moho to a depth of 100 km). The general structure of the layers was based on the velocity model of Moscoso et al. (2011). This structure includes several density discontinuities (e.g. ∼3000 kg/m^3 to ∼3200 kg/m^3 at the oceanic Moho) and other interfaces that correspond to changes in the density gradient (e.g. between the upper and lower oceanic crust). The first profile modeled was the PG3 (constrained by the velocities of Moscoso et al., 2011). The other profiles were modeled by modifying the model for PG3, first making small changes to the west of the trench in order to model the long wavelength differences in the gravity at the western segment of the profiles and then modifying the continental wedge density structure to fit data for profiles PG1, PG2, PG4 and PG5.

Due to the tradeoff between the geometry and density of the bodies in a gravity model, constraints obtained from independent geophysical data are necessary. In particular, we used the slab the SLAB1 model (Hayes et al., 2012) as a reference for the deep portion of the slab geometry (depth $\gtrsim$15–20 km) and seismic reflection data at shallower depths. For profile PG3, where the densities are controlled by Vp velocities (Moscoso et al., 2011), the geometry of SLAB1 explains the gravity anomaly. Results are similar for PG2 and PG4 (also located in the HSP zone); our models thus provide validation of the SLAB1 geometry. For profile PG5, the free-air gravity anomaly due to the continental wedge is clearly greater than that observed to the north, and the SLAB1 model shows an increase of the subducted slab angle at depths $\gtrsim$15–20 km compared to the others modeled profiles. We conducted an analysis of the sensitivity of the P5 model to slab dip. It is important to note that the SLAB1 model is not consistent with the slab depth at the trench observed in seismic reflection data for profile PG5, and our preferred model has been corrected to account for this.

We perturbed the slab depth by ±5 km compared to our preferred model. Fig. 6 shows that in a modified version of the profile PG5 (segmented black line in Figs. 6f and 6g), which has the same slab geometry as the preferred version of PG4 (magenta solid line), the densities and the corresponding vertical loading are greater than for profiles located to the north. For vertical loading, the modified model for profile PG5 is similar to the preferred model for profile PG1 (blue solid line), but clearly greater than for the preferred version of profiles PG2, PG3 and PG4 (red, green, and magenta solid lines), i.e., the profiles located at the HSP of the Maule earthquake. This implies that the increase of the continental wedge vertical load to the south of the HSP is directly supported by the increase of the gravity signal, and is not exclusively associated to the geometry of the SLAB1 model.

For this study, we are primarily interested in the region from 50 km to 150 km. The onshore portion of the gravity model corresponds to a $5' \times 5'$ resolution grid generated from the EGM2008 global gravity model (Sandwell and Smith, 2009). Because of this low resolution, the onshore segments of the models show only regional gradients representative of the crustal structure of the South-America plate.

Figs. 6a to 6e show the marine portion of the continental wedge in profiles PG1 to PG5 in more detail. In all profiles, the gravity signal is consistent with a wedge structure comprised of three units: (1) a frontal and shallow unit with densities of 2000–2500 kg/m^3, (2) an intermediate region with densities of 2500–2750 kg/m^3, and (3) an internal zone with densities >2750 kg/m^3.

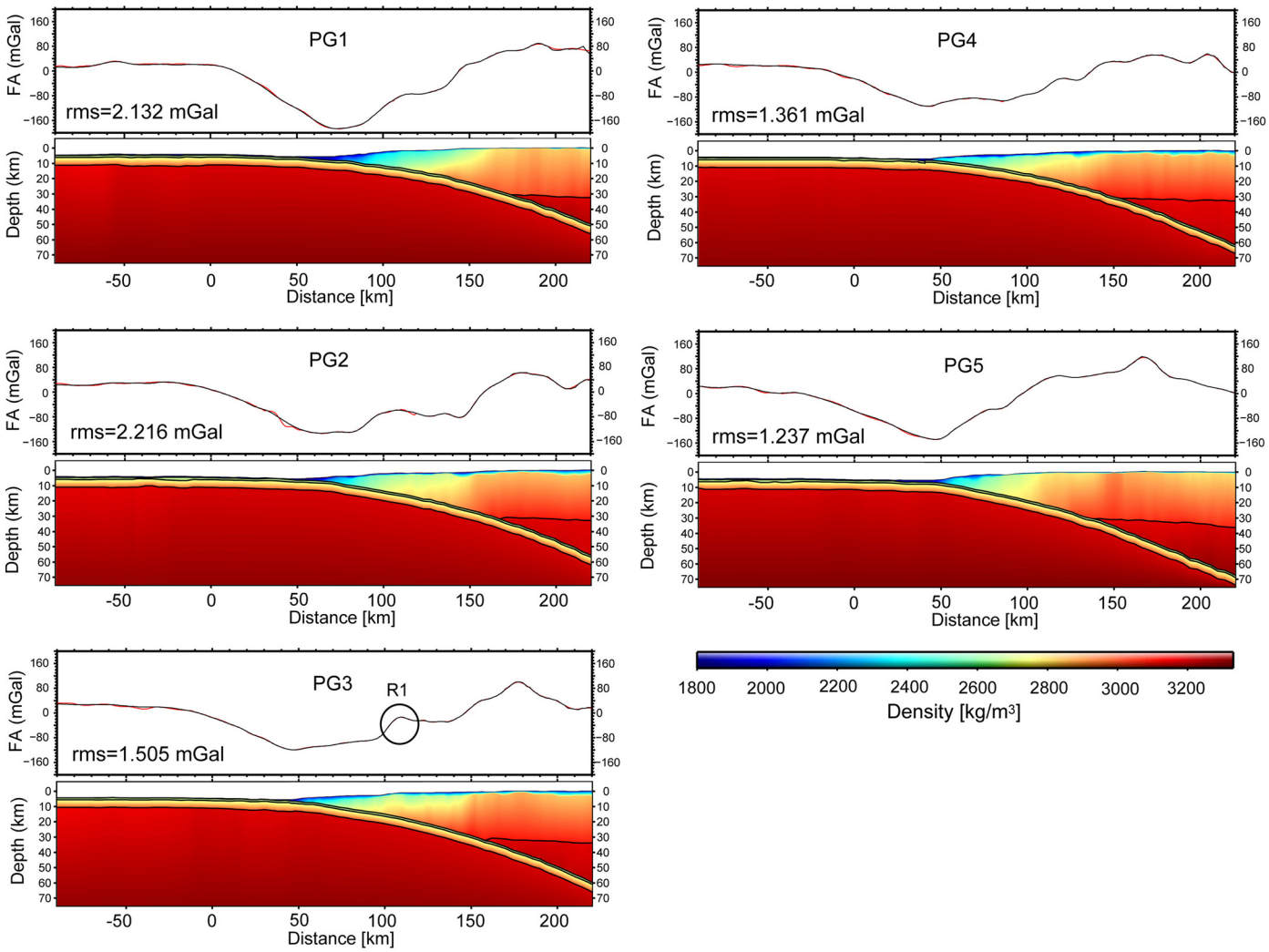

Fig. 5. Results of the gravity modeling for the five selected profiles (PG1 to PG5, see location in Fig. 3). For each profile, the upper panel shows the observed free-air gravity anomaly (red curve) and the modeled free-air gravity anomaly (black curve). The corresponding density-depth model is shown in the lower panel. The water layer is shown in white. The black circle on profile PG3 shows the location of a local gravity maximum (R1) that is shown in map view in Fig. 2. (For interpretation of the references to color in this figure legend, the reader is referred to the web version of this article.)

Fig. 6c shows that in the profile PG3, a shallow unit with low density (<2500 kg/m^3) and a variable thickness (<4 km) was included in the model to represent the sedimentary unit observed in the seismic tomography of Moscoso et al. (2011). Assuming initially that this shallow sedimentary unit is present in all profiles with similar internal densities, we find that it is thickest in profiles PG2, PG3 and PG4, consistent with the well-developed shelf basin overlying the continental basement in the zone of the HSP that was highlighted in the gravity data corrected for bathymetry effects (Fig. 2c).

In Figs. 6a to 6e, the 2500 kg/m^3 and 2750 kg/m^3 contours are shown to highlight the internal density structure of the continental basement. On profile PG3 a high density anomaly is observed overlying the interplate contact; ~60 km landward of the deformation front (R1 in Fig. 6c). This anomaly corresponds to the local gravity maximum interpreted as a possible subducted seamount in Fig. 2b. The free air anomaly associated with this body is shown in Fig. 5c. The model of profile PG2 (Fig. 6b), located ~30 km north of PG3, suggests that the R1 anomaly continues to the north, suggesting that this body has an elongated shape in the North–South direction with a maximum thickness located near the profile PG3. Approximately 30 km south of PG3, this anomaly is not observed (PG4, Fig. 6d). The location of the R1 anomaly roughly correlates with the presence of the magnetic high observed in the northern portion of the HSP zone (M1 in Fig. 2d), which can be an evidence of the oceanic genesis of the dense body observed over the subducted slab. A simple interpretation of the R1 anomaly is the subduction of a seamount, but alternative options are also possible, like the obduction of a dense unit during the ancient accretionary process that generated the paired metamorphic belt observed at the coast of the studied zone.

If we analyze the average densities of the continental wedge model, a regional pattern becomes evident. The curves in Fig. 6f, correspond to the densities averaged vertically from the seafloor to the interplate contact for the five profiles. Each profile shows a frontal unit with an average density <2400–2500 kg/m^3 that can be interpreted as the frontal accretionary prism. Beneath the middle slope, the average densities for PG5 are clearly higher than those for the other 4 profiles.

Using the modeled densities, we calculated the vertical loading over the interplate contact for the five gravity profiles (Fig. 6g) including the weight of the water column and of the continental wedge. The vertical load over the contact is similar for profiles PG1 to PG4, with values that range from ~100 MPa at the deformation front to ~900 MPa near the coast. In contrast, for profile PG5 the

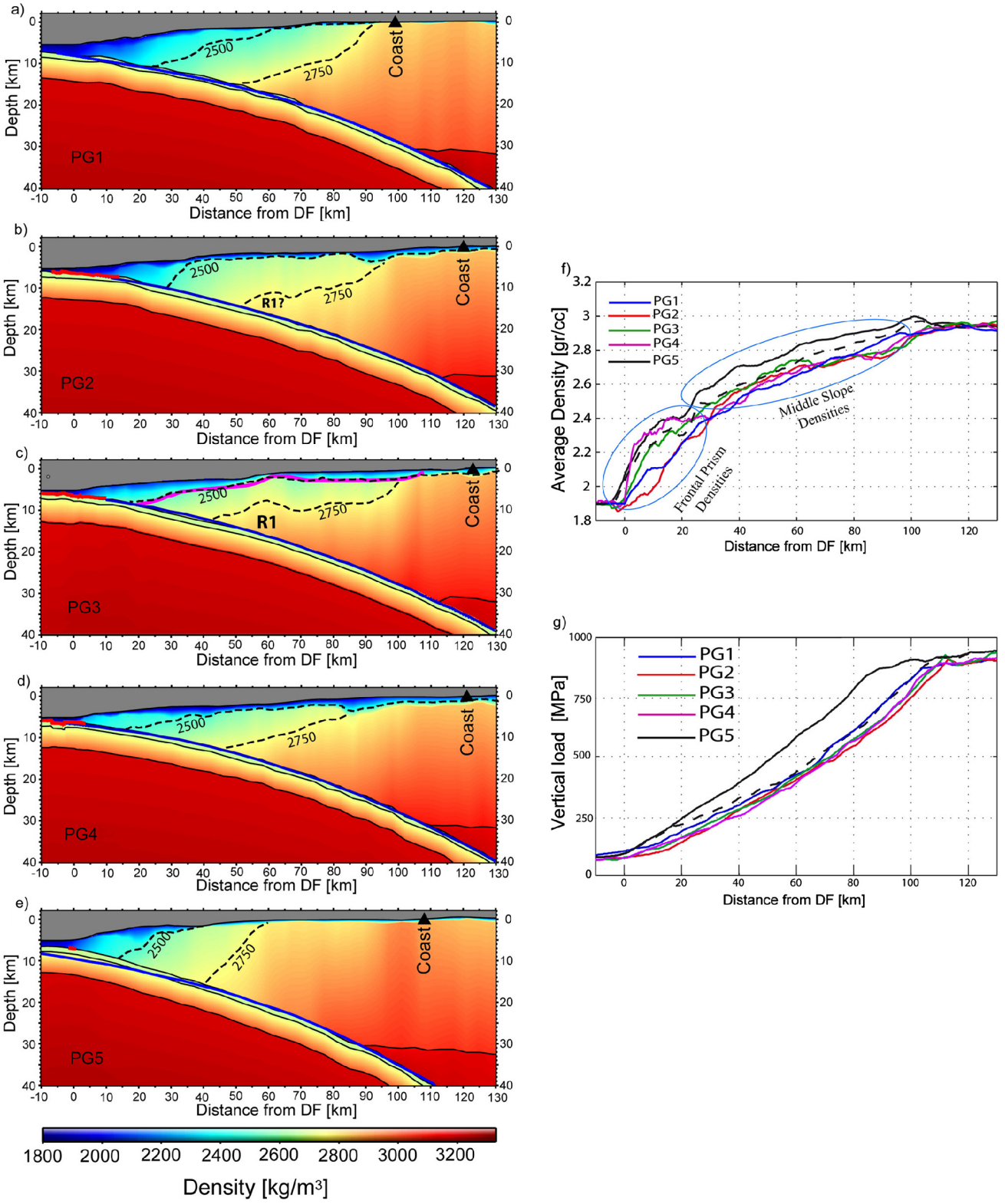

Fig. 6. Density model of the continental wedge. **(a)** Density-depth model of the profile PG1. Dashed curves correspond to the contours of 2500 kg/m^3 and 2750 kg/m^3 at the frontal part of continental wedge. The black triangle corresponds to the position of the coast. Dotted blue curve shows the SLAB1 model (Hayes et al., 2012) for the geometry of the subducting Nazca plate. The zero position of the horizontal scale corresponds to the location of the deformation front. **(b)** Density-depth model for profile PG2. Red line corresponds to the top of the oceanic crust derived from a coincident ChilePEPPER seismic profile. R1? indicates the possible location of a high density anomaly above the subducted slab. **(c)** Density-depth model for profile PG3. Red curve corresponds to the top of the oceanic crust derived from a coincident ChilePEPPER seismic profile. R1 indicates the location of a high density anomaly above the subducted slab. Magenta curve corresponds to the sediment–basement interface according to coincident wide-angle refraction seismic profile (Moscoso et al., 2011). **(d)** Density-depth model for profile PG4. Red curve corresponds to the top of the oceanic crust derived from a coincident ChilePEPPER seismic profile. **(e)** Density-depth model for profile PG5. Red curve corresponds to the top of the oceanic crust derived from a coincident seismic profile of the FONDEF Project DOOI104. **(f)** Vertically averaged density of the continental wedge for each of the five modeled profiles (see the explanation in the main text). **(g)** Vertical loading of the slab for each of the five modeled profiles (see the explanation in the main text). (For interpretation of the references to color in this figure legend, the reader is referred to the web version of this article.)

lateral gradient of the vertical load is considerably higher, resulting in a significantly larger load compared to the northern profiles.

We thus demonstrate that the northern portion of the rupture zone of the Maule earthquake, which includes the HSP area, was located beneath a segment of the margin where the continental wedge exhibits low average densities, which generate a low vertical load on the seismogenic contact. By using a similar approach, Tassara (2010) has shown that the HSP area of the giant Valdivia-1960 Mw9.5 earthquake was spatially correlated to a zone of low vertical load on the seismogenic contact, which in addition to our results, suggests a direct impact of the density and geometry of the continental wedge on the rupture processes of megathrust earthquakes.

5. Estimation of the basal friction

The slope angle (α) and slab angle (β) have been used to classify margins tectonically as erosive, non-accretionary and accretionary (Lallemand et al., 1994; Clift and Vannucchi, 2004). This classification is supported by the Non-Cohesive Coulomb Wedge theory (NCCW), where the angles α and β, and the direction of the principal stresses are related to frictional parameters (internal friction μ, effective basal friction μ_b^*), the density of the wedge (ρ_s), and the Hubbert–Rubey fluid pressure ratio (λ) which are controlled by the fluid pressure in the wedge (Dahlen, 1984). According to this model, accretionary wedges with low α values are associated with low values of μ_b^* and exhibit thrust faults with relatively high angles.

The static deformation style predicted by the NCCW theory for an unbroken and homogeneous wedge explains the structural features observed on many margins (e.g. Dahlen et al., 1984; Zhao et al., 1986; MacKay, 1995; Kopp and Kukowski, 2003; Polonia et al., 2007) and in sandbox experiments (e.g. Gutscher et al., 1996; Mourgues and Cobbold, 2006a). However, it is necessary to consider that the building of a fold and thrust belt is a cumulative process that involves short-term events such as landward fault rotation, generation of out-of-sequence thrusts, and episodic intervals of erosion due to the subduction of bathymetric highs or a decrease in the amount of sedimentary fill in the trench (Gutscher et al., 1996; Dominguez et al., 2000; Simpson, 2010). The rheological parameters estimated using the NCCW theory can therefore represent the long-term tectonic conditions for a continental wedge, but they do not necessarily describe short-term deformation processes like the coseismic rupture during the earthquakes.

In order to analyze latitudinal variations in the long-term tectonic conditions around the HSP, we use NCCW theory to estimate the effective basal friction necessary to explain the taper angles (α and β) observed in profiles PG1, PG3 and PG5. It is possible to divide the continental wedge in three sectors based on the angles of the seafloor and subducting plate: (1) the lower slope that starts at deformation front, (2) the middle slope that ends at the shelf break, and (3) the continental shelf (Fig. 7). For each sector we calculate the average densities from the 2-D gravity models and assume internal friction parameters based on expected geology. Because sector 1 is interpreted to be a frontal accretionary prism, we assume an internal fiction $\mu = 0.4790$ as appropriate for sandstone (Barton and Choubey, 1977). For sectors 2 and 3, interpreted to be continental basement, we use a value appropriate for granite $\mu = 0.5085$ (Barton and Choubey, 1977).

Table 1 shows our estimates of the effective basal friction for each sector in the three profiles. Different values of μ_b^* were calculated for the case of a dry wedge ($\lambda = 0$), hydrostatic pressure ($\lambda = \rho_{water}/\rho_s$), and the value of $\lambda = 0.67$ reported for the Taiwan margin by Dahlen (1984).

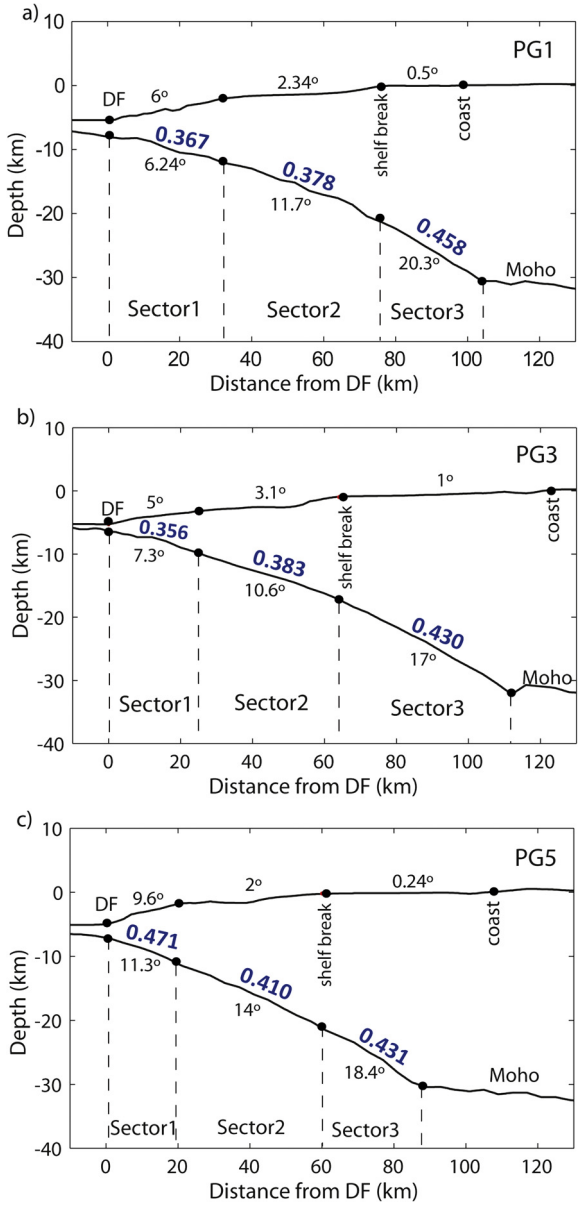

Fig. 7. Estimation of the effective basal friction coefficient according to the non-cohesive Coulomb wedge theory. The analysis was performed for profiles PG1, PG3 and PG5. The wedge was divided in three sectors (1, 2 and 3), which were simplified and modeled as independent wedges with constant basal and taper angles (shown in black). Blue numbers correspond to the modeled effective basal friction in the case of a wedge characterized by hydrostatic internal pressure (see the parameters and complementary results at Table 1). **(a)** Geometry and results for the profile PG1. **(b)** Geometry and results for the profile PG3. **(c)** Geometry and results for the profile PG5. (For interpretation of the references to color in this figure legend, the reader is referred to the web version of this article.)

Profiles PG1 and PG3 show low values of effective basal friction (<0.41) at the lower and middle slopes (sectors 1 and 2), and higher values (>0.43) for sector 3. In contrast, all sectors of the profile PG5 show high values of effective basal friction (>0.41). Furthermore, the highest values of the basal friction for profile PG5 are located in sector 1. These results indicate that the geometry and densities of the continental wedge in the vicinity of the HSP are consistent with low effective basal friction below the slope compared to the southern profile.

The estimates of the effective basal friction coefficient derived here for the gravity profiles, confirm the more general analysis of the NCCW parameters presented by Cubas et al. (2013b). Using a smoothed version of ETOPO1 bathymetry and the slab geometry

Table 1
Estimation of the effective basal friction coefficient according to the non-cohesive Coulomb wedge theory. The analysis was performed at the northern (PG1), central (PG3) and southern (PG5) gravity profiles. The wedge was divided in three sectors (see Fig. 7), which were simplified and modeled as independent wedges with constant taper and basal angles (α and β). Additionally we calculated average taper and basal angles calculated from the deformation front (DF) to the shelf break (SB). The values of the effective basal friction coefficient (blue numbers) were calculated in the cases of: a dry wedge ($\lambda = 0$), hydrostatic internal pressure ($\lambda = \rho_w/\rho_s$), and for the parameters observed in Taiwan ($\lambda = 0.67$, Dahlen, 1984). The average densities were extracted from the gravity models, and the values of internal friction (μ) were extracted from Barton and Choubey, 1977 (see details in the text).

PG1	α (°)	β (°)	ρ_s (kg/m^3)	μ	$\lambda = 0$	$\lambda = \rho_w/\rho_s$	$\lambda = 0.67$
Sector 1	6.00	6.24	2200	0.4790	0.337	0.367	0.405
Sector 2	2.34	11.60	2610	0.5085	0.369	0.378	0.399
Sector 3	0.50	20.30	2610	0.5085	0.457	0.458	0.461
From DF to SB	3.90	9.34	2430	0.5085	0.366	0.384	0.414
PG3	α (°)	β (°)	ρ_s (kg/m^3)	μ	$\lambda = 0$	$\lambda = \rho_w/\rho_s$	$\lambda = 0.67$
Sector 1	5.00	7.30	2230	0.4790	0.331	0.356	0.390
Sector 2	3.10	10.60	2600	0.5085	0.371	0.383	0.410
Sector 3	1.00	17.00	2600	0.5085	0.426	0.430	0.436
From DF to SB	3.80	9.30	2500	0.5085	0.358	0.380	0.411
PG5	α (°)	β (°)	ρ_s (kg/m^3)	μ	$\lambda = 0$	$\lambda = \rho_w/\rho_s$	$\lambda = 0.67$
Sector 1	9.60	11.30	2300	0.4790	0.456	0.471	0.479
Sector 2	2.00	14.00	2700	0.5085	0.403	0.410	0.425
Sector 3	0.24	18.40	2700	0.5085	0.430	0.431	0.433
From DF to SB	4.60	13.00	2500	0.5085	0.439	0.451	0.477

from SLAB1, they modeled the entire rupture area of the Maule earthquake and found a decrease of the effective basal friction coefficient at the HSP.

6. Discussion

The complexities of earthquake rupture processes during a megathrust earthquake can be explained by a combination of factors such as the inhomogeneous distribution of the accumulated stresses and the inhomogeneous rheological conditions at the seismogenic contact. Considering only the rheological factor, there is an apparent contradiction between the location of the HSP of Maule earthquake and the coincident decrease in wedge density and vertical loading on the seismogenic contact (also noted by Song and Simons, 2003, for the Aleutian margin). A local decrease in the vertical loading on the seismogenic contact can be related to a decrease of the normal and shear stresses if friction is homogeneous for the entire contact. Song and Simons (2003) concluded that the effect of the apparent decrease in normal stress could be balanced by an increase in the friction coefficient at the contact in order to increase the shear stress. This conclusion, however, is not consistent with our conclusion that the HSP is characterized by a low friction coefficient. Cubas et al. (2013a, 2013b) also concluded that the friction coefficient for the HSP in both the Maule and the 2011 Mw9.0 Tohoku–Oki earthquakes was characterized by low basal friction based on bathymetry and NCCW theory. Similarly, Fagereng (2011) studied the Hikurangi subduction zone (New Zealand) and concluded that the southern segment of that margin has a low basal friction coefficient and a high degree of interseismic coupling. In the case of the Maule earthquake, Metois et al. (2012) used GPS data to determine high coupling before the event in the zone that then ruptured, and the works of Moreno et al. (2010, 2012) show a zone of relatively low coupling only in the southern portion of the HSP. Our results, combined with those of Cubas et al. (2013a, 2013b) and Fagereng (2011), suggest that the combination of low basal friction and high slip during earthquakes is a common feature of subduction zone faults.

If we speculate that the long-term basal friction coefficient is related to the static and/or kinematic friction coefficient during the earthquake (short-term), then the HSP was developed in a zone of low coseismic shear stress. It is well known that the average coseismic slip can be related to the static stress-drop (e.g. considering a slip weakening model), but not with the initial and final stresses, which are not constrained by the seismological observations. On the other hand, the total potential energy change during the earthquake (W) (total work during the rupture) is a function of the average coseismic slip, the average stress and the surface area of the rupture (Kanamori, 1994; Wyss and Molnar, 1972):

$$W = S\frac{1}{2}(\sigma_0 + \sigma_1)D \tag{3}$$

where S is the surface area of the rupture, D is the average slip, σ_0 is the initial stress and σ_1 is the final stress after the rupture. We can express the stresses as a function of the normal stress, in the form proposed by Zielke and Arrowsmith (2008):

$$W = S\sigma_n\frac{1}{2}(\mu_0 + \mu_1)D \tag{4}$$

where, σ_n is the normal stress, μ_0 is the initial friction coefficient and μ_1 is the final friction coefficient. Considering that the normal stress is approximately constant during the seismic cycle, Eq. (4) suggests that high slip is not necessarily associated with a high value of coseismic work. In fact, if the normal stress and/or the average friction coefficient have a low value, the slip can be high without an increment of the total work. Even though relationship (4) cannot be extended directly to analyze the complex rupture processes (Rivera and Kanamori, 2005), using this relationship we can imagine, for example, a seismogenic zone with a homogeneous distribution of shear stresses and similar coseismic energy released by the zones involved in the earthquake, but with inhomogeneous slip distribution in response to variation of the normal stresses and/or the average friction coefficient below the continental wedge. This argument can be used to explain, at least partially, the features observed in the Maule earthquake, where the highest slip is located in a zone of low vertical loading (a component of the normal stress) and is spatially correlated with a zone of low long-term basal friction coefficient. However, a physical model to predict the coseismic slip as a function of previously measurable parameters has not yet been developed.

Fig. 8 shows the location of the high density anomaly observed on profile PG3 (R1), magnetic anomalies, aftershocks and the location of the 20 m slip contour according to the models of Moreno

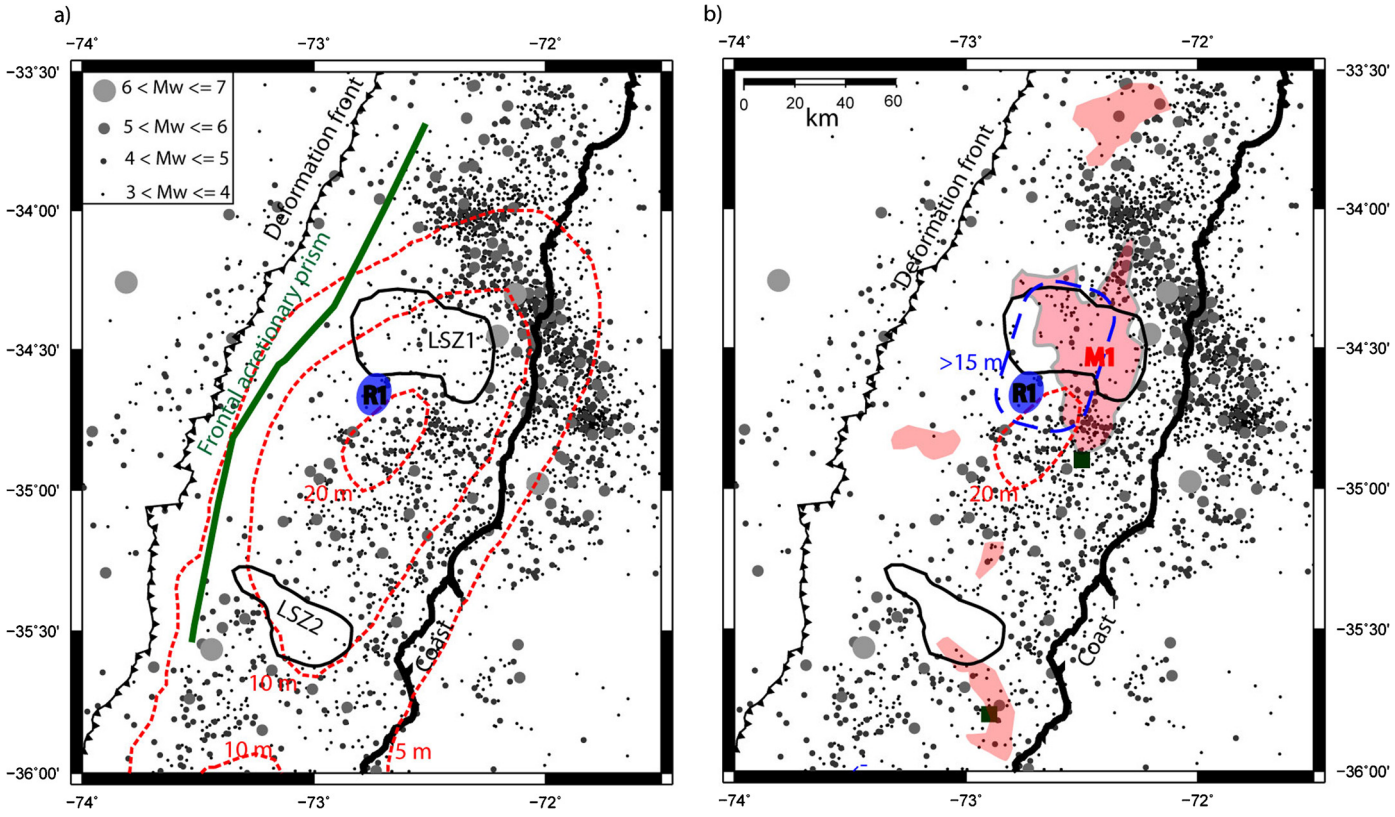

Fig. 8. Correlation of density and magnetic anomalies with seismological features of the Maule earthquake. Circles correspond to the aftershocks (observed during 1 year after the main event). **(a)** Dashed red lines are iso-contours of the slip according to Moreno et al. (2012). Green curve indicates the limit between the frontal accretionary wedge and the backstop according to the modeled gravity profiles. The areas LSZ1 and LSZ2 are zones of low aftershock seismicity and the blue area corresponds to the location of the high density anomaly R1. **(b)** Circles correspond to aftershocks. The dashed red curve is the iso-contour of 20 m slip according to Moreno et al. (2012). The dashed blue curve is the iso-contour of 15 m slip according to Luttrell et al. (2011). The blue area corresponds to the location of the high density anomaly (R1), and the red areas are the magnetic highs from the continental wedge. M1 is a large magnetic high that is spatially correlated with a zone of low aftershock seismicity (LSZ1). The green squares show the location of high frequency radiation asperities of the Maule earthquake according to Ruiz et al. (2012). (For interpretation of the references to color in this figure legend, the reader is referred to the web version of this article.)

et al. (2012) and Luttrell et al. (2011). The high density anomaly (R1) and the magnetic anomalies located landward of the accretionary prism (e.g. M1) are indicative of inhomogeneous lithology of the continental basement.

The potential relationship between the coseismic slip and aftershock distribution with local inhomogeneities in the upper plate depends on the nature of the observed anomalies and their function as barriers or asperities. As we can see in Fig. 8b, if the slip model of Moreno et al. (2012) is considered, then anomalies R1 and M1 are located north of the zone of greatest slip (20 m red contour in Fig. 8b). In contrast, for the model of Luttrell et al. (2011) these anomalies are located inside the highest slip zone (15 m blue contour in Fig. 8b). In the second case, the anomalies of high density and magnetization correlate with a local asperity in the middle of the HSP zone. In fact, if the high density anomaly R1 corresponds to a local increase of the contact friction, then the R1 anomaly can work as an asperity where a relatively high stress is concentrated in the interseismic period and released as high slip during the earthquake (Cloos, 1992; Watts et al., 2010). Moreover, using cGPS signals and strong motion records of the Maule earthquake, Ruiz et al. (2012) determined the source of two short-period coseismic pulses interpreted as locations of asperities. The northernmost of these sources is located ∼30 km landward of the high density anomaly (Fig. 8b), which considering the uncertainties of the seismological localization, could be interpreted as the same asperity.

As was mentioned before, a possible interpretation of the local R1 anomaly is the subduction of a seamount. According to Wang and Bilek (2011), the subduction of a seamount can lead to unfavorable conditions for developing a large earthquake and acts as a barrier to rupture propagation, at least in the outer accretionary complex. R1 clearly was not a barrier during the Maule earthquake, which suggests either that this local feature does not correspond to a seamount or that the local anomaly was too small to stop the large stress release of this megathrust earthquake. The density model of the PG3 profile (Fig. 6c) and the coincident depth-velocity tomography model of Moscoso et al. (2011) do not show thickening of the slab below R1 as was discussed by Kodaira et al. (2000) in Japan, but according to the age of the Nazca Plate in the zone (30–35 Myr, Müller et al., 2008), the root of R1 can be small (<1 km) like that observed by Kopp et al. (2004) below O'Higgins seamount ∼170 km to the north of the studied zone. We think that the most likely explanation for R1 is a seamount (probably decapitated) obducted to the continent, although it could also be a prolongation of highly magnetized continental basement.

In spite of uncertainties in the aftershock locations and the unconstrained magnetization vectors, which preclude modeling of the continental magnetic anomalies, there is a remarkable spatial correlation between the biggest patch of low aftershock seismicity (LSZ1 in Fig. 8b) and the large magnetic high (M1 in Fig. 8b) in the continental wedge above the HSP. We speculate that the magnetic anomaly results from a distinctive lithology in the continental basement that is relatively rigid compared to the surrounding lithologies. If we adopt the slip model of Luttrell et al. (2011), the highest slip zone (15 m blue contour in Fig. 8b) encompasses the LSZ1 and the R1 and M1 anomalies (Fig. 8b), which

suggests that aftershocks are distributed around a local asperity in the rupture area. This relationship is less pronounced if we adopt the slip model of Moscoso et al. (2011). Uncertainties in slip and inter-seismic coupling models and in aftershock locations are currently too large for a definitive correlation between fault behavior and detailed geologic structure. However, as these uncertainties decrease through accumulation of new data and improved analysis techniques, a better understanding of the impact of geological structure on rupture processes will be possible.

7. Conclusions

On a regional scale, 2-D gravity modeling and the analysis of bathymetric profiles indicates that the patch of greatest slip during the Maule earthquake is located in a segment of the margin characterized by (1) low densities in the continental wedge, (2) low vertical loading over the seismogenic contact, (3) a well-developed shelf basin, and (4) low taper angles consistent with a low effective basal friction coefficient.

This type of regional correlation has been observed in other subduction zones and supports the idea that segments of the margin with different long-term histories can act as distinct segments with different mechanical properties during the coseismic rupture process.

We interpret the correlation observed between high slip on the plate boundary during an earthquake, low vertical loading above the plate boundary and a low effective friction coefficient on the plate boundary in terms of the expression for the total potential energy change during the earthquake. This analysis suggests that if the normal stress and/or the frictional coefficient are low, high slip is not imply a high value of coseismic work.

Locally, the model shows the presence of a high density anomaly that correlates with the zone of highest slip, and we interpret this as a local asperity in the rupture area due to the obduction of a decapitated seamount or a seaward prolongation of a rigid continental basement over the seismogenic contact. Details of the relationship between local geologic structures in the forearc, inter-seismic coupling, slip during plate boundary earthquakes, and aftershock activity, however, remain ambiguous, and a process-based understanding will require that uncertainties in all of these characteristics of a subduction margin be resolved more accurately.

The results motivate detailed studies of the density anomalies in the continental wedge in segments of the convergent margins where slip models are available and in zones of seismic gaps as part of the tectonic framework necessary for future seismotectonic interpretation.

Acknowledgements

This work was funded by CONICYT (Comisión Nacional de Ciencia y Tecnología) under the program Development of Research Projects between Chile and the United Sates CONICYT grant #USA2012-001. Andrei Maksymowicz gratefully acknowledges a scholarship granted by the Chilean National Science Cooperation (CONICYT). Anne Tréhu thanks the U.S. National Science Foundation Marine Geology and Geophysics program for support for ChilePEPPER data acquisition and analysis through grant OCE1130013 to Oregon State University. Finally, we thanks the detailed comments formulated by the anonymous reviewers.

Appendix A. Supplementary material

Supplementary material related to this article can be found online at http://dx.doi.org/10.1016/j.epsl.2014.11.005.

References

Aki, K., 1979. Characterization of barriers on a earthquake fault. J. Geophys. Res. 84, 6140–6148.

Álvarez, O., Nacif, S., Gimenez, M., Folguera, A., Braitenberg, C., 2014. GOCE derived vertical gravity gradient delineates great earthquake rupture zones along the Chilean margin. Tectonophysics (ISSN 0040-1951). http://dx.doi.org/10.1016/j.tecto.2014.03.011.

Barrientos, S.E., Ward, S.N., 1990. The 1960 Chile earthquake: inversion for slip distribution from surface deformation. Geophys. J. Int. 103, 589–598. http://dx.doi.org/10.1111/j.1365-246X.1990.tb05673.x.

Barton, N.R., Choubey, V., 1977. The shear strength of rock joints in theory and practice. Rock Mech. 10 (1–2), 1–54.

Birch, F., 1961a. The velocity of compressional waves in rocks to 10 kilobars (Part I). J. Geophys. Res. 65, 1083–1102.

Birch, F., 1961b. The velocity compressional waves in rocks to 10 kilobars (Part 2). J. Geophys. Res. 66, 2199–2224.

Byrne, D.E., Davis, D.M., Sykes, L.R., 1988. Loci and maximum size of thrust earthquakes and the mechanics of the shallow region of subduction zones. Tectonics 7 (4), 833–857. http://dx.doi.org/10.1029/TC007i004p00833.

Clift, P., Vannucchi, P., 2004. Controls on tectonic accretion versus erosion in subduction zones: implications for the origin and recycling of the continental crust. Rev. Geophys. 42, RG2001. http://dx.doi.org/10.1029/2003RG000127.

Cloos, M., 1992. Thrust-type subduction-zone earthquakes and seamount asperities: a physical model for seismic rupture. Geology 20, 601–604.

Comte, D., Eisenberg, A., Lorca, E., Pardo, M., Ponce, L., Saragoni, R., Singk, S.K., Suarez, G., 1986. The great 1985 Central Chile earthquake: a repeat of previous great earthquakes in the region? Science 299, 449–453.

Contardo, X., Cembrano, J., Jensen, A., Diaz-Naveas, J., 2008. Tectono-sedimentary evolution of marine slope basins in the Chilean forearc (33°30′–36°50′S): insights into their link with the subduction process. Tectonophysics 459, 206–218.

Contreras-Reyes, E., Carrizo, D., 2011. Control of high oceanic features and subduction channel on earthquake ruptures along the Chile–Peru subduction zone. Phys. Earth Planet. Inter. 186, 49–58. http://dx.doi.org/10.1016/j.pepi.2011.03.002.

Contreras-Reyes, E., Flueh, E.R., Grevemeyer, I., 2010. Tectonic control on sediment accretion and subduction off south central Chile: implications for coseismic rupture processes of the 1960 and 2010 megathrust earthquakes. Tectonics 29, TC6018. http://dx.doi.org/10.1029/2010TC002734.

Contreras-Reyes, E., Jara, J., Maksymowicz, A., Weinrebe, W., 2013. Sediment loading at the southern Chilean trench and its tectonic implications. J. Geodyn.. http://dx.doi.org/10.1016/j.jog.2013.02.009.

Cordaro, E.G., Olivares, E., Galvez, D., Salazar-Aravena, D., Laroze, D., 2012. New He-3 neutron monitor for Chilean Cosmic-Ray Observatories from the Altiplanic zone to the Antarctic zone. Adv. Space Res. 49 (12), 1670–1683.

Cubas, N., Avouac, J.P., Leroy, Y.M., Pons, A., 2013a. Low friction along the high slip patch of the 2011 Mw 9.0 Tohoku–Oki earthquake required from the wedge structure and extensional splay faults. Geophys. Res. Lett. 40, 4231–4237. http://dx.doi.org/10.1002/grl.50682.

Cubas, N., Avouac, J.P., Souloumiac, P., Leroy, Y.M., 2013b. Megathrust friction determined from mechanical analysis of the forearc in the Maule earthquake area. Earth Planet. Sci. Lett. (ISSN 0012-821X) 381, 92–103. http://dx.doi.org/10.1016/j.epsl.2013.07.037.

Dahlen, F.A., 1984. Noncohesive critical Coulomb wedges: an exact solution. J. Geophys. Res. 89 (10), 125–133.

Dahlen, F.A., Suppe, J., Davis, D.M., 1984. Mechanics, of fold-and-thrust belts and accretionary wedges: cohesive Coulomb theory. J. Geophys. Res. 89, 10087–10101.

Dannowski, A., Grevemeyer, I., Kraft, H., Arroyo, I., Thorwart, M., 2013. Crustal thickness and mantle wedge structure from receiver functions in the Chilean Maule region at 35°S. Tectonophysics 592, 159–164. http://dx.doi.org/10.1016/j.tecto.2013.02.015.

Das, S., Watts, A.B., 2009. Effect of subducting seafloor topography on the rupture characteristics of great subduction zone earthquakes. In: Lallemand, S., Funiceillo, F. (Eds.), Subduction Zone Geodynamics. Springer-Verlag, Berlin–Heidelberg, pp. 103–118.

Davis, D., Suppe, J., Dahlen, F.A., 1983. Mechanics of fold-and-thrust belts and accretionary wedges. J. Geophys. Res. 88 (B2), 1153–1172.

Díaz-Naveas, J.L., 1999. Sediment subduction and accretion at the chilean convergent margin between 35°S and 40°S. Ph.D. thesis (Unpublished), Christian Albrechts-Universität zu Kiel. 130 p.

Dominguez, S., Malavieille, J., Lallemand, S.E., 2000. Deformation of accretionary wedges in response to seamount subduction: Insights from sandbox experiments. Tectonics (ISSN 0278-7407) 19, 0278–7407. http://dx.doi.org/10.1029/1999TC900055.

Fagereng, A., 2011. Wedge geometry, mechanical strength, and interseismic coupling of the Hikurangi subduction thrust, New Zealand. Tectonophysics 507, 26–30. http://dx.doi.org/10.1016/j.tecto.2011.05.004.

Fleming, S., Tréhu, A.M., 1999. Crustal structure beneath the central Oregon convergent margin from potential field modeling: evidence for a buried basement ridge in local contact with a seaward-dipping backstop. J. Geophys. Res. 104, 20431–20447.

Flueh, E.R., Bialas, J. (Eds.), 2008. RRS JAMES COOK Fahrtbericht. Cruise Report JC23-A & B: Chile-Margin-Survey, OFEG Barter Cruise with SFB 574; 03.03.–25.03. 2008 Valparaiso – Valparaiso, 26.03.-18.04.2008 Valparaiso – Valparaiso IFM-GEOMAR Report, 20. IFM-GEOMAR, Kiel, 242 pp. http://dx.doi.org/10.3289/ifm-geomar_rep_20_2008.

Gulick, S.P.S., Austin, J.A., McNeill, L.C., Bangs, N.L.B., Martin, K.M., Henstock, T.J., Bull, J.M., Dean, S., Djajadihardja, Y.S., 2011. Updip rupture of the 2004 Sumatra earthquake extended by thick indurated sediments. Nat. Geosci. http://dx.doi.org/10.1038/NGEO1176.

Gutscher, M.-A., Peacock, S.M., 2003. Thermal models of flat subduction and the rupture zone of great subduction earthquakes. J. Geophys. Res. 108 (B1), 2009. http://dx.doi.org/10.1029/2001JB000787.

Gutscher, M.-A., Kukowski, N., Malavieille, J., Lallemand, S., 1996. Cyclical behavior of thrust wedges: insights from high basal friction sandbox experiments. Geology 24 (2), 135–138.

Hamilton, E.L., 1978. Sound velocity–density relations in sea floor sediments. J. Acoust. Soc. Am. 63, 366–377.

Hayes, G.P., Wald, D.J., Johnson, R.L., 2012. Slab1.0: a three-dimensional model of global subduction zone geometries. J. Geophys. Res. 117, B01302. http://dx.doi.org/10.1029/2011JB008524.

Hayes, G.P., Bergman, E., Johnson, K.L., Benz, H.M., Brown, L., Meltzer, A.S., 2013. Seismotectonic framework of the 2010 February 27 Mw 8.8 Maule, Chile earthquake sequence. Geophys. J. Int. 195 (2), 1034–1051. http://dx.doi.org/10.1093/gji/ggt238.

Hervé, F., 1988. Late Paleozoic subduction and accretion in Southern Chile. Episodes 11, 183–188.

Hicks, S.P., Rietbrock, A., Haberland, C., Ryder, I.M.A., Simons, M., Tassara, A., 2012. The 2010 Mw 8.8 Maule, Chile earthquake: nucleation and rupture propagation controlled by a subducted topographic high. Geophys. Res. Lett. 39, L19308. http://dx.doi.org/10.1029/2012GL053184.

Hyndman, R.D., Yamano, M., Oleskevich, D.A., 1997. The seimogenic zone of subduction thrust faults. Isl. Arc 6, 244–260.

Jarvis, A., Reuter, H.I., Nelson, A., Guevara, E., 2008. Hole-filled SRTM for the globe Version 4, available from the CGIAR-CSI SRTM 90 m Database. http://srtm.csi.cgiar.org.

Kanamori, H., 1994. Mechanics of earthquakes. Annu. Rev. Earth Planet. Sci. (ISSN 0084-6597) 22, 2207–2237. http://resolver.caltech.edu/CaltechAUTHORS:KANareps94.

Kodaira, S., Takahashi, N., Nakanishi, A., Miura, S., Kaneda, Y., 2000. Subducted seamount imaged in the rupture zone of the 1946 Nankaido earthquake. Science 289, 104–106.

Kopp, H., Kukowski, N., 2003. Backstop geometry and accretionary mechanics of the Sunda margin. Tectonics 22 (6), 1072. http://dx.doi.org/10.1029/2002TC001420.

Kopp, H., Flueh, E.R., Papenberg, C., Klaeschen, D., 2004. Seismic investigations of the O'Higgins Seamount Group and Juan Fernández Ridge: aseismic ridge emplacement and lithosphere hydration. Tectonics 23, TC2009. http://dx.doi.org/10.1029/2003TC001590.

Lallemand, S.E., Schnurle, P., Malavieille, J., 1994. Coulomb theory applied to accretionary and nonaccretionary wedges—possible causes for tectonic erosion and/or frontal accretion. J. Geophys. Res. 99, 12033–12055.

Lange, D., Tilmann, F., Barrientos, S., Contreras-Reyes, E., Methe, P., Moreno, M., Heit, B., Agurto, H., Bernard, P., Vilotte, J.-P., Beck, S., 2012. Aftershock seismicity of the 27 February 2010 Mw 8.8 Maule earthquake rupture zone. Earth Planet. Sci. Lett. 317–318, 413–425. http://dx.doi.org/10.1016/j.epsl.2011.11.034.

Lay, T., Ammon, C.J., Kanamori, H., Koper, K.D., Sufri, O., Hutko, A.R., 2010. Teleseismic inversion for rupture process of the 27 February 2010 Chile (Mw 8.8) earthquake. Geophys. Res. Lett. 37, L13301. http://dx.doi.org/10.1029/2010GL043379.

Lomnitz, C., 1971. Grandes terremotos y tsunamis en Chile durante el periodo 1535–1955. Geofís. Panam. 1, 151–178.

Lorito, S., Romano, F., Atzori, S., Tong, X., Avallone, A., McCloskey, J., Cocco, M., Boschi, E., Piatanesi, A., 2011. Limited overlap between the seismic gap and coseismic slip of the great 2010 Chile earthquake. Nat. Geosci. 4, 173–177.

Luttrell, K.M., Tong, X., Sandwell, D.T., Brooks, B.A., Bevis, M.G., 2011. Estimates of stress drop and crustal tectonic stress from the 27 February 2010 Maule, Chile, earthquake: implications for fault strength. J. Geophys. Res., Solid Earth 116 (B11).

MacKay, M.E., 1995. Structural variation and landward vergence at the Toe of the Oregon Accretionary Prism. Tectonics 14, 1309–1320.

Maksymowicz, A., 2007. Modelo 3D del Moho bajo la zona de Chile central y oeste de Argentina (31°S–34°S), utilizando funciones de recepción, Tesis Magister en Ciencias, mención Geofísica. Universidad de Chile, Santiago, Chile. http://tesis.uchile.cl/handle/2250/116730.

Metois, M., Socquet, A., Vigny, C., 2012. Interseismic coupling, segmentation and mechanical behavior of the central Chile subduction zone. J. Geophys. Res. 117, B03406. http://dx.doi.org/10.1029/2011JB008736.

Moreno, M., Rosenau, M., Oncken, O., 2010. 2010 Maule earthquake slip correlates with pre-seismic locking of Andean subduction zone. Nature 467, 198–202. http://dx.doi.org/10.1038/nature09349.

Moreno, M., Melnick, D., Rosenau, M., Báez, J.C., Klotz, J., Oncken, O., Tassara, A., Bataille, K., Chen, J., Socquet, A., Bevis, M., Bolte, J., Vigny, C., Brooks, B., Ryder, I., Grund, V., Smalley, R., Carrizo, D., Bartsch, M., Hase, H., 2012. Toward understanding tectonic control on the Mw 8.8 2010 Maule Chile earthquake. Earth Planet. Sci. Lett. 321, 152–165.

Moscoso, E., Grevemeyer, I., Contreras-Reyes, E., Flueh, E.R., Dzierma, Y., Rabbel, W., Thorwart, M., 2011. Revealing the deep structure and rupture plane of the 2010 Maule, Chile earthquake (Mw = 8.8) using wide angle seismic data. Earth Planet. Sci. Lett. 307, 147–155. http://dx.doi.org/10.1016/j.epsl.2011.04.025.

Mourgues, R., Cobbold, P.R., 2006a. Thrust wedges and fluid overpressures: sandbox models involving pore fluids. J. Geophys. Res. 111, B05404. http://dx.doi.org/10.1029/2004JB003441.

Müller, R.D., Landgrebe, T.C.W., 2012. The link between giant earthquakes and the subduction of oceanic fracture zones. J. Geophys. Res., Solid Earth 3, 447–465. http://dx.doi.org/10.5194/se-3-447-2012. www.solid-earth.net/3/447/2012/.

Müller, R.D., Sdrolias, M., Gaina, C., Roest, W.R., 2008. Age, spreading rates, and spreading asymmetry of the world's ocean crust. Geochem. Geophys. Geosyst. 9 (4), Q04006. http://dx.doi.org/10.1029/2007gc001743.

Nakanishi, A., Kodaira, S., Park, J.-O., Kaneda, Y., 2002. Deformable backstop as seaward end of coseismic slip in the Nankai Trough seismogenic zone. Earth Planet. Sci. Lett. 203, 255–263.

Pacheco, J., Sykes, L., Scholz, C., 1993. Nature of seismic coupling along simple plate boundaries of the subduction type. J. Geophys. Res. 98, 14133–14159.

Polonia, A., Torelli, L., Brancolini, G., Loreto, M.-F., 2007. Tectonic accretion versus erosion along the southern Chile trench: oblique subduction and margin segmentation. Tectonics 26, TC3005. http://dx.doi.org/10.1029/2006TC001983.

Rietbrock, A., Ryder, I., Hayes, G., Haberland, C., Comte, D., Roecker, S., Lyon-Caen, H., 2012. Aftershock seismicity of the 2010 Maule Mw = 8.8, Chile, earthquake: correlation between co-seismic slip models and aftershock distribution? Geophys. Res. Lett. 39, L08310. http://dx.doi.org/10.1029/2012GL051308.

Rivera, L., Kanamori, H., 2005. Representations of the radiated energy in earthquakes. Geophys. J. Int. 162 (1), 148–155.

Ruegg, J.C., Rudloff, A., Vigny, C., Madariaga, R., de Chabalier, J.B., Campos, J., Kausel, E., Barrientos, S., Dimitrov, D., 2009. Interseismic strain accumulation measured by GPS in the seismic gap between Constitución and Concepción in Chile. Phys. Earth Planet. Inter. 175, 78–85. http://dx.doi.org/10.1016/j.pepi.2008.02.015.

Ruiz, S., Madariaga, R., Astroza, M., Saragoni, G.R., Lancieri, M., Vigny, C., Campos, J., 2012. Short period rupture process of the 2010 Mw 8.8 Maule earthquake in Chile. Earthq. Spectra 28 (S1), S1–S18.

Sandwell, D.T., Smith, W.H.F., 2009. Global marine gravity from retracked Geosat and ERS-1 altimetry: ridge segmentation versus spreading rate. J. Geophys. Res. 114, B01411. http://dx.doi.org/10.1029/2008JB006008.

Scholz, C.H., Campos, J., 1995. On the mechanism of seismic decoupling and back-arc spreading in subduction zones. J. Geophys. Res. 100, 22103–22115.

Simpson, G.D.H., 2010. Formation of accretionary prisms influenced by sediment subduction and supplied by sediments from adjacent continents. Geology 38 (2), 131–134.

Song, T.A., Simons, M., 2003. Large trench-parallel gravity variations predict seismogenic behavior in subduction zones. Science 301, 630–633.

Sparkes, R., Tilmann, F., Hovius, N., Hillier, J., 2010. Subducted seafloor relief stops rupture in South American great earthquakes: implications for rupture behavior in the 2010 Maule, Chile earthquake. Earth Planet. Sci. Lett. 298 (1–2), 89–94. http://dx.doi.org/10.1016/j.epsl.2010.07.029.

Tassara, A., 2010. Control of forearc density structure on megathrust shear strength along the Chilean subduction zone. Tectonophysics 495, 34–47.

Thornburg, T.M., Kulm, L.D., 1987. Sedimentation in the Chile Trench: depositional morphologies, lithofacies, and stratigraphy. Geol. Soc. Am. Bull. 98, 33–52.

Tréhu, A.M., Blakely, R.J., Williams, M.C., 2012. Subducted seamounts and recent earthquakes beneath the central Cascadia forearc. Geology 40, 103–106.

Wang, K., Bilek, S.L., 2011. Do subducting seamounts generate or stop earthquakes? Geology 39, 819–822.

Watts, A.B., Koppers, A.A.P., Robinson, D.P., 2010. Seamount subduction and earthquakes. Oceanography 23 (1), 166–173. http://hdl.handle.net/1957/15613.

Wells, R.E., Blakely, R.J., Sugiyama, Y., Scholl, D.W., Dinterman, P.A., 2003. Basin-centered asperities in great subduction zone earthquakes: a link between slip, subsidence, and subduction erosion? J. Geophys. Res. 108 (B10), 2507. http://dx.doi.org/10.1029/2002JB002072.

Willner, A.P., Thomson, S.N., Kröner, A., Wartho, J.A., Wijbrans, J., Hervé, F., 2005. Time markers for the evolution and exhumation history of a late Paleozoic paired metamorphic belt in central Chile (34°–35°30′S). J. Petrol. 46, 1835–1858.

Wyss, M., Molnar, P., 1972. Efficiency, stress drop, apparent stress, effective stress, and frictional stress of Denver, Colorado, earthquakes. J. Geophys. Res. 77 (8), 1433–1438.

Zhao, W., Davis, D.M., Dahlen, F.A., Suppe, J., 1986. Origin of convex accretionary wedges: evidence from Barbados. J. Geophys. Res. (ISSN 0148-0227) 91. http://dx.doi.org/10.1029/0JGREA000091000B10010246000001.

Zielke, O., Arrowsmith, J.R., 2008. Depth variation of coseismic stress drop explains bimodal earthquake magnitude – frequency distribution. Geophys. Res. Lett. 35, L24301. http://dx.doi.org/10.1029/2008GL036249.